UC Davis
UC Davis Previously Published Works

Title

Dual modality intravascular catheter system combining pulse-sampling fluorescence lifetime imaging and polarization-sensitive optical coherence tomography

Permalink

https://escholarship.org/uc/item/1g08z5tn

Journal

Biomedical Optics Express, 15(4)

ISSN

2156-7085

Authors

Bec, Julien
Zhou, Xiangnan
Villiger, Martin
et al.

Publication Date

2024-04-01

DOI

10.1364/boe.516515

Peer reviewed

Dual modality intravascular catheter system combining pulse-sampling fluorescence lifetime imaging and polarization-sensitive optical coherence tomography

JULIEN BEC,[1,†] XIANGNAN ZHOU,[1,†] MARTIN VILLIGER,[2] JEFFREY A. SOUTHARD,[3] BRETT BOUMA,[2] AND LAURA MARCU[1,*]

[1]*Biomedical Engineering, University of California, Davis, CA 95616, USA*
[2]*Wellman Center for Photomedicine, Massachusetts General Hospital and Harvard Medical School, Boston, MA 02114, USA*
[3]*Division of Cardiovascular Medicine, UC Davis Health System, University of California-Davis, Sacramento, CA 95817, USA*
[†]These authors contributed equally to this work
[*]*lmarcu@ucdavis.edu*

Abstract: The clinical management of coronary artery disease and the prevention of acute coronary syndromes require knowledge of the underlying atherosclerotic plaque pathobiology. Hybrid imaging modalities capable of comprehensive assessment of biochemical and morphological plaques features can address this need. Here we report the first implementation of an intravascular catheter system combining fluorescence lifetime imaging (FLIm) with polarization-sensitive optical coherence tomography (PSOCT). This system provides multi-scale assessment of plaque structure and composition via high spatial resolution morphology from OCT, polarimetry-derived tissue microstructure, and biochemical composition from FLIm, without requiring any molecular contrast agent. This result was achieved with a low profile (2.7 Fr) double-clad fiber (DCF) catheter and high speed (100 fps B-scan rate, 40 mm/s pullback speed) console. Use of a DCF and broadband rotary junction required extensive optimization to mitigate the reduction in OCT performance originating from additional reflections and multipath artifacts. This challenge was addressed by the development of a broad-band (UV-visible-IR), high return loss (47 dB) rotary junction. We demonstrate in phantoms, *ex vivo* swine coronary specimens and *in vivo* swine heart (percutaneous coronary access) that the FLIm-PSOCT catheter system can simultaneously acquire co-registered FLIm data over four distinct spectral bands (380/20 nm, 400/20 nm, 452/45 nm, 540/45 nm) and PSOCT backscattered intensity, birefringence, and depolarization. The unique ability to collect complementary information from tissue (e.g., morphology, extracellular matrix composition, inflammation) with a device suitable for percutaneous coronary intervention offers new opportunities for cardiovascular research and clinical diagnosis.

1. Introduction

Coronary artery disease (CAD) remains the worldwide leading cause of death [1]. In its most severe form, plaque rupture or erosion leads to the formation of a thrombus that occludes a coronary artery branch, resulting in a myocardial infarction [2]. Extensive research has identified common features of culprit plaques; for example, high plaque burden, a thin fibrous cap overlying a large lipid pool, and the presence of active inflammation [2]. Plaque formation and evolution, however, are dynamic processes with a complex interplay of stabilizing phenomena, such as the recruitment of smooth muscle cells and the formation of a collagen-rich extracellular matrix (ECM), and destabilizing phenomena, such as the proliferation of macrophage foam cells (mFC) and accumulation of necrotic material [2–4]. These features can only be investigated using

imaging catheters that provide simultaneous assessment of morphology and composition. Over the last decade, different combinations of imaging modalities providing morphological information (e.g., optical coherence tomography (OCT) and intravascular ultrasound (IVUS)) along with compositional information [5,6] (e.g., fluorescence lifetime imaging (FLIm) [7], near-infrared fluorescence (NIRF) [8] and autofluorescence (NIRAF) [9], near-infrared spectroscopy (NIRS) [10,11]) have been reported. While such hybrid intracoronary imaging systems have shown the ability to assess key plaque features such as lipid accumulation [5], inflammation, oxidative stress, and endothelial permeability [8], new hybrid imaging modalities capable of comprehensive assessment of plaques features conducive to acute myocardial infarction are needed [2,12,13].

Ultraviolet excitation time-resolved fluorescence spectroscopy (TRFS) [14] and its subsequent mesoscopic fluorescence lifetime imaging (FLIm) [15] implementation, have emerged as a means of evaluating the biochemical composition of atherosclerotic lesions. FLIm relies on the measurement of endogenous fluorescent molecule decay rates over multiple spectral bands associated with the emission of arterial vessels (e.g., collagen and crosslinks, elastin, lipid components, and ceroids). Earlier work conducted in *ex vivo* human coronary arteries has demonstrated that a combination of FLIm-derived optical parameters can identify mFC accumulation and the presence of superficial calcification and newly formed ECM [7,16]. Intravascular implementations in combination with intravascular ultrasound (IVUS) and OCT are a key step towards demonstrating the clinical utility of FLIm [17–19].

Intravascular OCT is an established technology and remains the most used clinical research tool in interventional cardiology for evaluating new treatment modalities [20]. It has played an important role in elucidating CAD-related pathobiological processes. Currently, it offers the highest spatial resolution for intravascular imaging, enables assessment of thin-fibrotic cap (associated with plaque rupture), and can elucidate aspects of plaque erosion. The recent adaptation of PSOCT [21,22] to measure the polarization of the backscattered IR light has demonstrated the ability to measure depth-resolved birefringence and depolarization with standard intravascular imaging catheters; thus, enhancing OCT's capabilities for plaque characterization. The PSOCT high-resolution backscatter images enable the identification of smooth muscle cells, collagen, and cholesterol crystals via birefringence, as well as necrotic and lipid-rich regions via depolarization [21]. PSOCT, however, cannot directly measure tissue composition. As demonstrated in numerous studies [7,14,16,23], FLIm has the ability to detect compositional features associated with ECM composition, mFC infiltration and necrotic material. Thus, the FLIm and PSOCT combination reported here for the first time provides not only a means for retrieving complementary features and better stratify critical plaque pathobiology but also for cross-validating biochemical features. Cross-validation is of particular relevance for future clinical validation in patients because no ground truth information (e.g., histology) will be available to corroborate the intravascular imaging findings.

Engineering of intravascular systems able to perform imaging in coronary arteries presents several challenges. First, the device must have a low profile (<1 mm) and high flexibility to cross atherosclerotic lesions and maintain structural integrity and imaging performance (low non-uniform rotation distortion) when placed in tortuous anatomy. Second, a high imaging speed (typically 100 frames/second) is required to limit cardiac motion artifacts and ensure that a full imaging pullback (typically 80-100 mm) can be performed during the blood clearing period following a bolus flush (2-3 s).

The study presented here focuses on the design and characterization of a dual modality catheter-based imaging system, first of its kind, able to simultaneously acquire FLIm and PSOCT data while addressing the challenges noted above. We evaluated key performance metrics of the dual-modality system and demonstrated its ability to acquire co-registered FLIm and PSOCT data in coregistration and birefringent phantoms. The reliability and usability of the system was tested in *ex vivo* coronary artery specimens and *in vivo* in swine heart in a coronary percutaneous

intervention setting. The catheter system reported here is compatible with a clinical setting, where it will enable a comprehensive image-based assessment of plaque pathophysiology, thus, improving our understanding of mechanisms underlying plaque formation and supporting the development of new therapies.

2. Methods

2.1. Integrated FLIm-PSOCT system

The FLIm-PSOCT system presented here builds on earlier work from our group demonstrating the integration of 2-channel pulse-sampling FLIm and conventional OCT. The FLIm-PSOCT catheter system reported here consists of a new 4-channel FLIm engine, a PSOCT engine and an optimized multimodal motor drive unit (MDU) and intravascular catheters (Fig. 1).
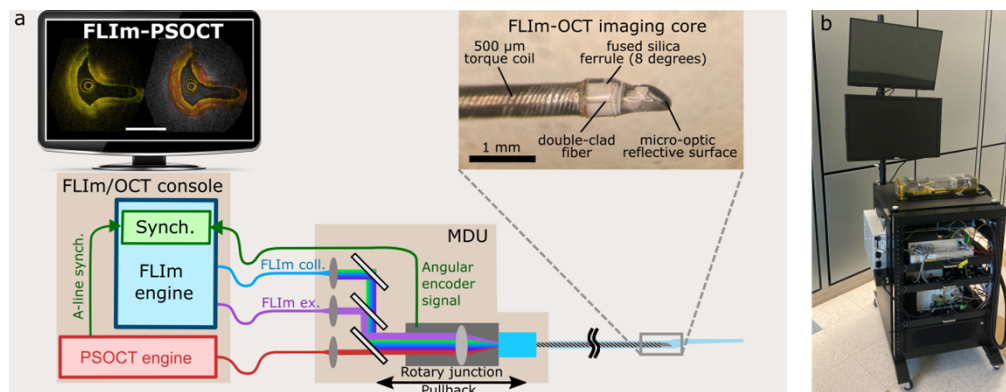

Fig. 1. Overall description of the hybrid intravascular imaging system. FLIm and PSOCT engines are located in the console. Actuation (rotation, pullback) of the motor drive unit (MDU) is controlled by the FLIm engine. Synchronization of FLIm data acquisition and PSOCT data acquisition is performed by the FLIm engine, where the PSOCT A-line synchronization signal and the rotation index of the MDU angular encoder are saved with a digitizer sharing a clock with the FLIm data acquisition. The catheter consists of a double-clad fiber (DCF) enclosed in a 2-layer torque coil. A fused silica ferrule improves reliability of the freeform micro-optic assembly by increasing the adhesive bond area, isolating the optics from forces that may be transferred by the torque coil, and preventing the micro-optics from contacting the sheath. An 8-degree angle at the interface with the micro-optics reduces the back-reflection of the optical adhesive interface (a). The FLIm-PSOCT system is packaged in a compact cart that can be easily transported to facilitate validation in animal model (b).

FLIm engine. The FLIm instrumentation was based on a pulse sampling technique, where the entire fluorescence decay is obtained for each excitation pulse [24]. An instrumental setup developed by our group for clinical validation of FLIm in intraoperative settings [25] was adapted to intravascular use. Specifically, fluorescence excitation light was provided by a free-running pulsed 355-nm diode-pumped solid-state laser (32 kHz repetition rate, 2-µJ pulse energy, SNV-60P-100, TEEM photonics, France) and delivered to the MDU using a 50-µm core multimode fiber (FG050UGA, Thorlabs, NJ). The fluorescence emission signal was spectrally resolved and detected in four distinct spectral bands using a set of filters and dichroic (380/20 nm, 400/20 nm, 452/45 nm, 540/50 nm) and individual photodetector modules (APD430A2-SP1, Thorlabs, NJ, United States). Each module was composed of a UV-enhanced avalanche photodiode, biasing circuitry able to vary the detector gain between M = 1 to >500, and a trans-impedance amplifier. Sampling of the detector signals is performed at 6.25 GS/s by two synchronized high-speed

digitizers (NI PXIe-5185, National Instruments, TX). To improve SNR, a moving average of five lifetime values is used.

Polarization Sensitive OCT engine. A polarization-modulated, fiber-based frequency domain PSOCT setup derived from a 1310 nm swept-source OCT system (Soleron, NH, USA) was used in this study. The PSOCT engine consists of a wavelength-swept laser (HSL-200-50LC, Santec Corp., Japan) with a center wavelength of 1310 nm, a wavelength scanning range of 105 nm, and an A-line acquisition rate of 50 kHz. This results in a full width at half maximum of the intensity point spread function, i.e., the squared norm of the reconstructed tomogram of a single reflector, of ~9 µm in tissue, assuming a refractive index of 1.34. The system utilized a polarization modulation scheme, in which the source polarization state was alternated for consecutive A-lines to illuminate the sample with polarization states located orthogonal to each other on the Poincaré sphere. This modulation scheme precludes the need for phase stability between A-lines, as reconstruction is performed in the incoherent Stokes formalism. This was achieved using a customized fiber-based high-speed phase retarder (Boston Applied Technologies, United States) synchronized with the swept-source laser and positioned between the laser source and the OCT interferometer. To ensure a constant reference signal, the modulated polarization states were adjusted with a polarization controller, following the polarization modulator but still before splitting into sample and reference arms, to project equally onto the linear polarizer in the reference arm input to the polarization-diverse receiver. The output of the dual balanced detectors (PDB410C, Thorlabs Inc, USA) was digitized at 200 MS/s (ATS9352, AlazarTech, Pointe-Claire, Canada). A 50 MHz acousto-optic frequency shifter in the reference arm resolved depth degeneracy leading to a full imaging depth of 13.2 mm in air.

MDU. The MDU's design was derived from an earlier implementation [19], with some key differences. Briefly, optical coupling between PSOCT and FLIm engines and the catheter's imaging core was performed using individual stationary collimators for PSOCT, FLIm excitation, and FLIm collection, aligned with a rotary collimator to which the catheter imaging core was connected (Fig. 1). A first adjustable dichroic mirror (F735-Di02-25 × 36, Semrock, NY, United States) was used to combine PSOCT and FLIm beams, whereas a second adjustable dichroic mirror (Di01-R355, Semrock, NY, United States) was used to combine FLIm excitation and emission pathway (Fig. 1).

The rotary collimator was composed of a stationary air bearing (OAV0500IB, NJ, United States), a custom rotating shaft housing an adjustable lens and custom fiber receptacle, combined with a closed loop motion control itself composed of a brushless motor (EC-max 22, Maxon motors, Sachseln, Switzerland), optical encoder mounted on the collimator shaft (US Digital, Vancouver, WA, United States), and speed controller (ESCON 24/2, Maxon Motors, Sachseln, Switzerland). The index channel of the optical encoder was acquired by a dedicated digitizer card to enable accurate reconstruction of FLIm and PSOCT B-scans.

The use of individual stationary collimators enables the compensation of the chromatic focal shift observed in the shared rotary collimator lens over the 355-1370 nm spectral range required for FLIm and OCT operation [18]. A 3-mm long fused silica optical wedge, which presents an 8-degree facet that matches the angle of the catheter core's APC connectors was integrated into the catheter connector receptacle. This additional element ensured that the optical beam and fiber connector were concentric with the collimator's rotation axis while providing separation between the location of the Fresnel reflection of the receptacle and the focal plane of the rotary collimator. The purpose of this design was to limit the coupling of the reflected light into the OCT stationary fiber (Fig. 2).

Imaging catheter. The catheter was composed of a double-clad fiber (SM-9/105/125-20A, Nufern, CT, United States), enclosed in a 500-µm outer diameter torque coil (Asahi Intecc, Aishi, Japan), terminated at the proximal end with a stainless-steel shaft and an SC/APC connector. OCT is performed via the DCF's core whereas the inner cladding is used to transmit both
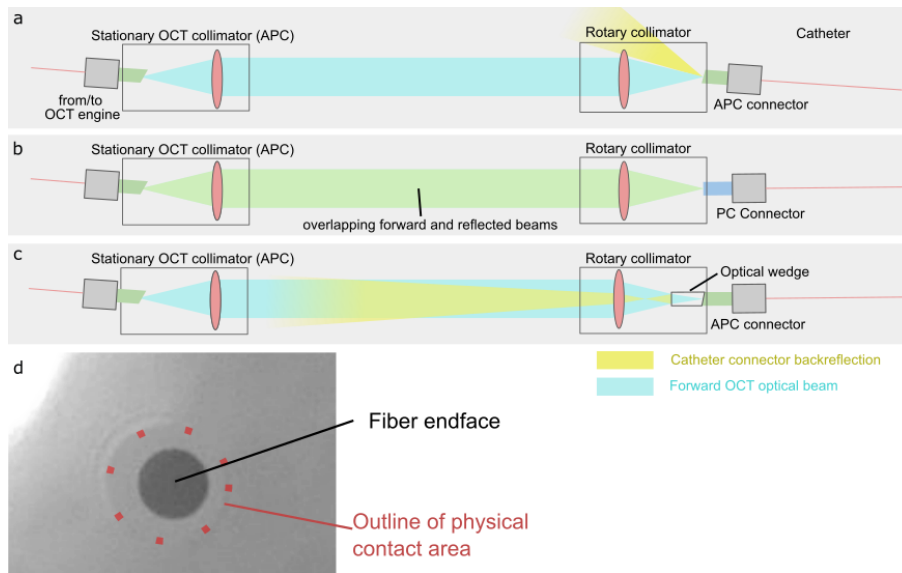
Fig. 2. **Schematic of free-space fiber coupling between stationary OCT collimator and rotary catheter collimator** (steering mirrors omitted for simplicity). APC to APC junction provides the highest return loss but requires the catheter connector to be angled by 4 degrees to ensure efficient coupling (a). This configuration is mechanically imbalanced and not suitable for high-speed rotation. APC to PC rotary junction adopted in earlier implementation ensures that optical beam and catheter connector are concentric with the rotation axis, but the back reflection observed in the catheter proximal fiber facet leads to a low return loss of ~14 dB, negatively affecting the system sensitivity (b). The fiber receptacle of the rotary collimator used for the FLIm-PSOCT system presented an additional cylindrical "wedge" element with an 8-degree interface with the catheter APC connector, keeping the rotation assembly balanced (c). With this design, the back-reflection generated from the air/glass interface occurs on the proximal end of the wedge, far from the collimator's focal plane, which ensures high return loss (44 dB). The APC interface between the distal face of the wedge and the catheter connector ensures that return losses remain high even if physical contact were to be lost due to wear or contamination of that interface. This design is suitable for simultaneous UV/Vis/NIR operation and does not require any index matching fluid. Close-up of the interface between the catheter connector and the wedge, imaged through the wedge, visualizing the area of physical contact between the angle-polished domed ferrule and the wedge. Its extension beyond the cladding ensures that the insertion of the wedge is not leading to reduction in the optical coupling efficiency to and from both core and inner cladding of the DCF (d).

fluorescence excitation and fluorescence emission. The distal end of the catheter consisted of an angle-polished fused silica spacer and freeform reflective optic with a working distance of ~1.2 mm [26]. The catheter sheath was terminated by a 2.7 Fr (0.92 mm) outer diameter transparent polymethylpentene imaging window (Mitsui Chemicals, Tokyo, Japan). The sheath was flushed with saline solution before use.

2.2. Data reconstruction

FLIm. The fluorescence decay parameters from each FLIm point measurement were retrieved using a constrained least-square deconvolution with Laguerre expansion (CLSD-LE) method [27]. This approach provides average lifetime values for each spectral band and captures more complex decay dynamics from a mixture of fluorophores, as expected from atherosclerotic lesions.

Computationally, this method was shown to be more time-efficient than the multiexponential approaches. En-face images were obtained by combining FLIm point measurements obtained between consecutive timestamps as part of the same 360-degree rotation. Detailed investigation of the FLIm average lifetime variation with signal intensity in phantom and arteries was performed by binning FLIm measurements based on signal intensity and computing the mean and standard deviation of the averaged lifetime for each intensity bin.

Reconstruction of OCT backscattered intensity, tissue birefringence and degree of polarization. Conventional structural OCT and PSOCT images were obtained simultaneously from the raw datasets offline. Birefringence is the unitless ratio of retardation per propagation distance. It corresponds to the difference in refractive indices (Δn) experienced by light polarized parallel and orthogonal to the fibrillary tissue components. Depth-resolved tissue birefringence was reconstructed using spectral binning [28] to mitigate artifacts caused by polarization mode dispersion originating from the fiber optic components of the imaging system. The spectral binning algorithm employed bins of 1/5th of the original spectral bandwidth and a lateral (circumferential) Gaussian filter for averaging Stokes vectors with a full width at half maximum (FWHM) corresponding to a catheter rotation angle of 8.64° (6 A-lines per input polarization state). Birefringence was retrieved by computing the retardance φ between adjacent depth-pixels and converted to birefringence with $\Delta n = \varphi \lambda_c / (4\pi \Delta z)$, where λ_c is the center wavelength in air, and $\Delta z = 4.81$ μm the axial separation between adjacent pixels in a medium with refractive index n = 1.34. Areas of high depolarization, which precludes the reconstruction of meaningful birefringence, are omitted from the visualization maps as stated in the following section.

Depolarization corresponds to a randomization of the detected polarization states within the small neighborhood around each pixel defined by the Gaussian filtering of Stokes vectors. It is expressed as the ratio of the depolarized signal to the total intensity. Depolarization (D) was computed as the complement to 1 of the degree of polarization. Depolarization is always in the range of 0 (completely polarized) to 1 (completely random and depolarized).

All processing steps were implemented in Matlab 2022a (Mathworks Inc., Natick, Massachusetts) with an Intel Core i9-12900 k processor, 64 GB of RAM and GPU acceleration (RTX 3090, Nvidia).

Birefringence visualization. To merge the color-mapped birefringence and reflectance image with the gray scale reflection image in regions of high depolarization, the birefringence color image was weighted with $w = [1/2 - \text{erf}\{(D - 2/3)/0.08\}]$, where erf is the error function. The gray-scale image was scaled with the complementary weight $1-w$, and then the two images were added. The final rendering visualizes the tissue structure, enhanced with the tissue birefringence mapped to color, and indirectly specifies regions of high depolarization in grayscale.

Image reconstruction and display. OCT and FLIm measurements for each B-scan were determined based on timestamps obtained from the rotary collimator's angular encoder index channel, corresponding to the start of each consecutive catheter rotation. Timestamps for PSOCT data were generated by acquiring the OCT digitizer's synchronization output with the same digitizer card as the rotation index, thus providing shared timestamps across both modalities. Structural OCT, tissue birefringence, and depolarization were computed and displayed as stated above. For each FLIm spectral band, hybrid FLIm-OCT B-scans were generated by color-coding each OCT A-line by the average lifetime value at that angular location.

2.3. Phantom and ex vivo coronary specimen imaging

The technical performance (coregistration, sensitivity, imaging range) of the dual imaging catheter was benchtop evaluated on tissue phantom and on excised coronary specimens. FLIm-OCT coregistration was evaluated in a 3-mm inner diameter tubular fluorescent acrylic phantom where a stent was placed to provide clearly identifiable features. Birefringence evaluation was performed using a custom phantom consisting of birefringent (polymer) positioned in a

3D-printed structure. DCF artifacts observed in the OCT image were characterized using a 0.5-mm thick ABS (Acrylonitrile Butadiene Styrene) sheet. Imaging of coronary artery vessels was performed using a healthy swine heart obtained from the UC Davis meat lab, a federally inspected meat processing plant. The segment used for imaging consisted of the left ostium, left main and left anterior descending artery. A 0.014" guidewire was placed in the artery to guide the imaging catheter and removed prior to imaging to allow full visualization of the vessel without guidewire shadow. Before and during imaging, the healthy swine coronary artery was kept in saline solution.

2.4. In vivo coronary imaging in swine

The intravascular FLIm-PSOCT catheter system was tested *in vivo* in a healthy swine model: (i) to demonstrate that the DCF catheter can be placed in coronary arteries, (ii) to confirm that blood clearance in the imaged artery segment is achievable using safe flushing procedure with low molecular weight Dextran solution, (iii) to evaluate the effect of vessel size on FLIm data quality.

In vivo testing was conducted in accordance with the Guide for the Care and Use of Laboratory Animals [29]. The Institutional Animal Care and Use Committee at the University of California, Davis approved the study for the use of Yorkshire cross swine. Animal care and use was performed by qualified individuals and supervised by veterinarians. All facilities and transportation complied with current legal requirements and guidelines. Anesthesia was used in all surgical interventions. Our animal facilities meet the standards of the American Association for Accreditation of Laboratory Animal Care.

The animal (65 kg, 10 weeks) was subjected to general anesthesia and the FLIm-PSOCT catheter was introduced via the femoral artery using a modified Seldinger technique into the left anterior descending and left circumflex coronary artery under fluoroscopy guidance through a standard 7 French guiding catheter and a 7 French guide extension, over a 0.014 inch guidewire.

At each location, multiple pullback scans were acquired in vessel diameters ranging from 1.5 mm to 3.5 mm using non-occlusive flush (4 to 6 cc/s for 5 s) of low molecular weight Dextran solution (10% LMD in 5% Dextrose, Hospira, IL).

2.5. Tissue exposure computation

Tissue exposure was computed according to IEC 60825 / ANSI Z136.1 [30,31]. UV-A (FLIm excitation) and IR-A (OCT) are to be considered additive. Single-pulse UV exposure was assessed by computing the irradiance at the FLIm excitation beam waist and comparing it with the maximum permissible exposure (MPE) of skin of $3 * 10^{10} W/m^2$ obtained from IEC 60825 (Table A.5). For UV single-pulse exposure, the OCT light contribution was omitted because its average power is multiple orders of magnitude smaller than the UV peak power. The OCT optical power of the proposed FLIm-PSOCT system is 13 mW, or about 50% of clinical intravascular OCT systems, so the UV MPE for multiple overlapping UV pulses during rotation was derated to 50% of the single wavelength MPE value. The multiple UV pulses exposure was assessed by first computing the maximum number of overlapping UV pulses at the surface of the catheter and ensuring that the average power for this train of pulses was below the derated MPE. Full detail of the calculation is available in Supplement 1.

3. Results

3.1. Integrated FLIm-PSOCT system

We designed and engineered a dual FLIm-PSOCT catheter imaging system able to simultaneously acquire tomographic structure, depth-resolved birefringence and cumulative depolarization, and surface fluorescence lifetime measurements over four distinct spectral bands from the luminal surface. The bi-modal catheter's small diameter of 2.7 Fr (1.65 m length) assures compatibility
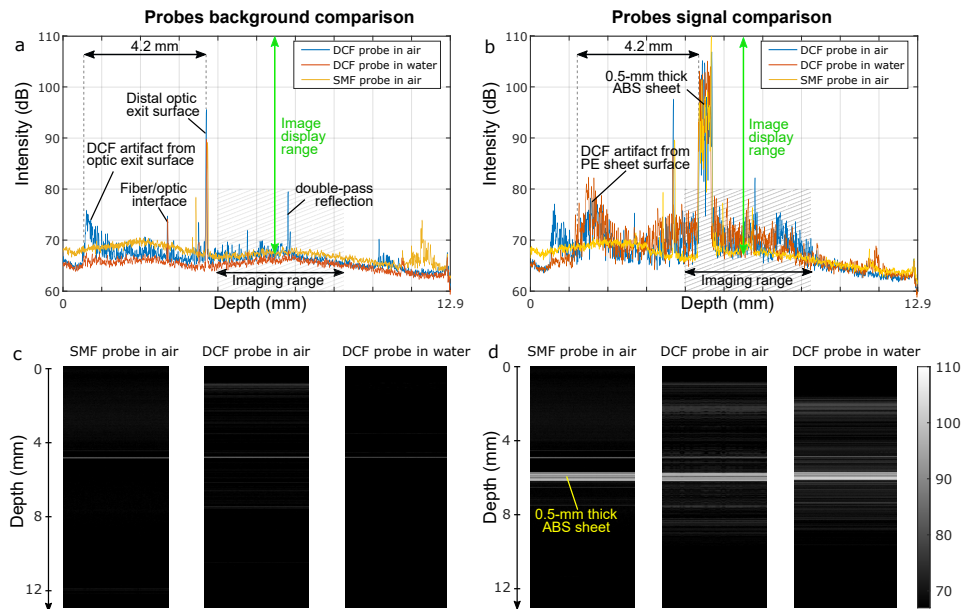
Fig. 3. OCT background and signal analysis. The OCT background was measured for the FLIm-PSOCT DCF imaging core in air, in water and for a reference single-mode commercial OCT catheter imaging core. The delay was set to maximize the sensitivity where tissue is expected to be present during use (a). Sharp reflections from the fiber to distal optics are visible for the DCF probe, reflection from the distal optics exit face is clearly visible for all probes. A DCF artifact caused by the inner-cladding propagation of light backscattered at the exit surface is observed when the DCF core is tested in air. The maximum distance between exit surface and DCF artifact of 4.2 mm is consistent with what is expected from the catheter length and core and inner cladding mismatch. When tested in water, the reflection from the distal optics exit surface is reduced by approximately 10 dB and the associated DCF artifact is suppressed. In that configuration, the background of the FLIm-PSOCT DCF imaging core is better than what is obtained from a clinical imaging core that relies on a single-mode fiber. Imaging of a 0.5-mm thick ABS sheet demonstrates that both probes lead to similar sensitivities (b). The DCF artifact caused by the sample starts 4.2 mm closer than the object. It leads to 2-4 dB additional noise in the imaging region compared to the SMF probe. Images of background and test object demonstrates that despite the presence of DCF artifacts, the DCF probe provides images comparable to the reference SMF probe (c,d).

with intravascular interrogation of coronary arteries. The MDU enables a catheter rotation of 100 rps and a pullback length of 100 mm at up to 40 mm/s pullback speed, values similar to clinical OCT for which blood displacement during imaging is achieved with a bolus flush. The FLIm engine, also located in the console, contains a 32 kHz repetition rate 355-nm laser, leading to 320-point measurements per OCT B-scan. FLIm detection is achieved by individual avalanche photodiode detectors for each of the four spectral bands of the instrument (380/20 nm, 400/20 nm, 452/45 nm, 540/45 nm) allowing independent control of the detector gain for each spectral channel, thus enabling optimization of SNR for each individual channel. The OCT engine located in the console contains a polarization-modulated light source with a sweep rate of 50 kHz that enables 500 OCT A-lines per rotation. Polarization information is obtained by alternating the polarization state for each A-line, combined with polarization-diverse balanced detection, yielding 250 pairs of polarization-resolved measurements used to extract birefringence and depolarization information. Synchronization of FLIm and OCT is a key aspect to ensure proper coregistration of

the multimodal data. Both FLIm and PSOCT light sources are free-running and if a fixed number of measurements per B-scan is used, drifts in the FLIm laser repetition rate or OCT sweep rate could lead to loss of coregistration. We addressed this issue by generating timestamps for the catheter rotation, FLIm point measurements, and PSOCT a-lines. PSOCT data was acquired with a digitizer that did not share the same clock as the FLIm and rotation index digitizer. This limitation, however, was addressed by acquiring the OCT digitizer's synchronization output with the same digitizer card as the rotation index.

3.2. Rotary collimator performance

The integration of the optical wedge in the rotary junction's catheter connector receptacle leads to an ~800-fold reduction of the reflected optical power originating from the rotary junction compared to the reference design with an UPC-connectorized catheter (from 287 μW to 0.35 μW), corresponding to a 29 dB increase of the return loss. This return power value is close to the return power observed without any catheter present and leads to an identical baseline noise in the OCT image (see Supplement 1 and Table S1). This result was achieved without adversely impacting the single-mode coupling efficiency of >70%. As observed in Fig. 2(d), the axial preload of the catheter connector ensures a physical contact that extends beyond the double-clad fiber facet, ensuring that no additional Fresnel losses are incurred by the insertion of this element in the optical path.

3.3. Double-clad fiber induced artifacts

The use of a DCF for coherent detection is a well-known challenge for PSOCT and OCT implementation. DCFs reduce the quality of OCT by introducing multipath artifacts due to the crosstalk between inner cladding modes and the fundamental core mode occurring at different coupling interfaces [32,33]. Such crosstalk is expected to generate a ghost image, whose location is determined by the length of the DCF and differences between the group velocity of the core mode and different cladding modes. Because more than one cladding mode is typically involved, the ghost image appears spread along the imaging depth. Modal distributions in step-index double-clad fibers are complex and are actively studied [33–35] but their behavior can be approximated by considering that the inner cladding modes are not affected by the core. Under this assumption, the minimum and maximum path differences that determine the ghost image location are determined by the following equations:

$$\Delta Z_{min} = (n_{innercladding} - n_{core}) * L_{fiber} \tag{1}$$

$$\Delta Z_{max} = (n_{innercladding}/\cos\theta_{max} - n_{core}) * L_{fiber} \tag{2}$$

where θ_{max} is the maximum angle to the fiber axis of a ray guided in the inner cladding. Using the parameters of the DCF (see Supplement 1), $\Delta Z_{min} = -4.62$ mm, whereas $\Delta Z_{max} = 18.37$ mm, with light guided in the lowest order cladding mode propagating faster than the core mode, causing a negative delay, and light propagated in the highest order cladding mode traveling slower than the light in the core. Experimentally, we observed that both the exit surface of the catheter as well as objects imaged with the device generate DCF artifacts (Fig. 3). Most of the ghost image is located at a shorter pathlength with respect to the distal optics exit surface, with a maximum path difference of approximately 4.2 mm, in good agreement with the expected location computed from Eq. (1) that predicts a path difference of 4.6 mm. These results are also in good agreement with more thorough characterization of ghost images using the same DCF [33]which reported a ghost displacement of ~2.3 mm/m, corresponding to 3.8 mm for a 1.65-m long catheter. In addition to this most prominent part of the ghost image, likely caused by crosstalk through the lowest order cladding modes, the higher order cladding modes cause ghost image artifacts at larger pathlengths, even beyond the fundamental image, yet with an

amplitude of only 2 to 4 dB. These findings are consistent with the expectation that only the lower modes of the inner cladding effectively couple back into the single-mode core of the stationary fiber. None of these DCF-induced artifacts seem to create specific issues with birefringence and depolarization measurements, as the images obtained from the birefringence phantom are in close agreement with images acquired with the reference PSOCT system (see below). Birefringence values observed from artery specimens are also consistent with contrast expected from healthy vessels [21].

3.4. Performance assessment in phantoms

The results of FLIM-PSOCT co-registration accuracy evaluated in the fluorescent phantom with stent are depicted in Fig. 4. The stent struts are visible in the OCT maximum intensity projection and the strut shadows are seen in the en-face FLIm intensity image. FLIm and OCT are inherently spatially co-registered as both FLIm and OCT beams are concentric, and the accurate overlap of FLIm and OCT images demonstrates proper synchronization of both imaging modalities.
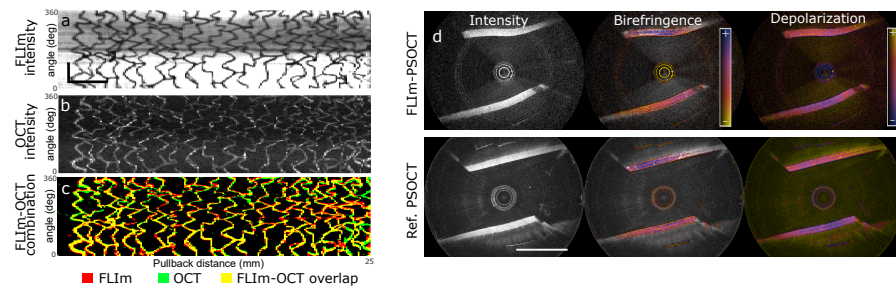

Fig. 4. Coregistration and birefringence phantom. A stent deployed in a fluorescent acrylic tubular phantom provided both FLIm (a) and OCT contrast (b). Binary masks were generated from FLIm intensity and OCT backscattered intensity and combined to demonstrate registration (c). Both modalities are spatially registered since FLIm and OCT optical beams are concentric, but synchronization of both subsystems is required to achieve accurate coregistration, as demonstrated in the overlap en face image. Imaging of the birefringence phantom was performed for the FLIm-PSOCT hybrid system and a reference PSOCT system [21]. Both systems are able to characterize the layered birefringence of the polymer sheets. Scale bars: 3 mm.

The performance of the current hybrid system relative to a reference PSOCT intravascular imaging system earlier reported [36] was evaluated in a phantom consisting of a birefringent film of stretched scattering polycarbonate [37] held in place by a 3D printed holder. As expected, the DCF used for the construction of the hybrid catheter presents crosstalk between the cladding and core modes. That locally increases the noise floor at characteristic pathlength positions within the OCT image [18,32,38] compared to a PSOCT-only reference system. While the DCF artifacts are apparent in the structural OCT signal, they have less impact on the reconstruction of birefringence and depolarization images. The strong birefringence of the polycarbonate film is clearly revealed, contrasting with the lower birefringence of the supporting material. Depolarization increases for more oblique imaging angles, both in the multimodal and the reference system.

3.5. Performance assessment in swine coronary artery ex vivo

Demonstrating the performance of the hybrid system in artery specimens is key to ensure that FLIm and PSOCT parameters can be extracted from samples with optical properties (fluorescence, absorption, scattering, birefringence, depolarization) that are similar to the target application. The OCT backscatter intensity image demonstrates clear visualization of arterial morphological

structure (media, adventitia, and perivascular tissue), with a penetration depth of at least 1 mm (Fig. 5(c)). In healthy animals, the intima typically consists of a single layer of endothelial cells, which thickness is less than the axial resolution of OCT and is therefore not visible. The strong smooth muscle cell content in the media generates high birefringence in conditions where the optical beam is normal to the vessel wall (Fig. 5(d)). As expected, the demarcation between media and adventitia based on birefringence is less clear when the optical beam crosses the media at a shallow angle. Specifically, in that configuration, the optic axis of the birefringent tissue is more closely aligned with the beam directly and thus less birefringence is detected. As expected from healthy coronary arteries, the depolarization is low and uniformly distributed across the artery cross-section (Fig. 5(d)). En-face average lifetime FLIm maps demonstrate predominant emission in the 380, 400, and 450-nm bands, as expected from healthy vessels, with uniform average lifetime and intensity ratio (380/20 nm band lifetime: 6.021 ± 0.130 ns, 400/20 nm band lifetime: 5.891 ± 0.157 ns, 452/45 nm band lifetime: 5.766 ± 0.124 ns, 540/45 nm band lifetime: 4.803 ± 0.248 ns).

3.6.   Intracoronary imaging in swine in vivo (percutaneouse intervention)

Bimodal data obtained in the left anterior descending coronary artery is presented in Fig. 6. The fluorescence intensity (Fig. 6(a)) maps show that a large fluorescence signal variation (from <0.2 V to 0.75 V) can be observed during a full catheter rotation due to change of catheter to artery wall distance. Consistent lifetime values are observed in the average lifetime maps (Fig. 6(b)) except for locations where the signal intensity falls below a threshold of approximately 0.2 V. The bimodal FLIm-PSOCT images confirmed that a good flush with Dextran solution is achieved during the entire pull back distance. The tunica media layer, characterized by a high smooth muscle cells content presents a high birefringence value is clearly visible in the PSOCT image, as expected for healthy swine. Plots of peak FLIm intensity versus average fluorescence lifetime (Fig. 6(f)) confirm that lifetime can be measured consistently with a peak intensity higher than approximately 0.2 V. The lifetime measurement standard deviation increases with lowering signal intensity as expected.

3.7.   Tissue exposure evaluation

Tissue exposure during normal use of the system is compliant with IEC 60825/ ANSI Z136.1 [30,31]. Indeed, safety factors of 2.47 and 3.87 were obtained for single UV pulse exposure and multiple overlapping pulses for a combination of UV and IR beams, respectively. Details about the calculations are available in Supplement 1.
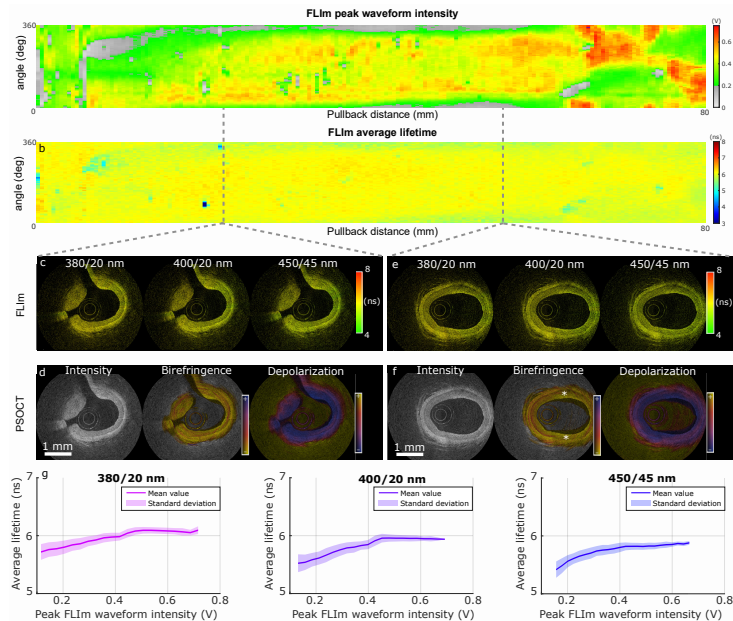
Fig. 5. *Ex vivo* **FLIm-PSOCT imaging of swine coronary artery segment.** Demonstrating the performance of the hybrid system in artery specimen is key to ensure that FLIm and PSOCT parameters can be extracted from samples with optical properties (fluorescence, scattering, birefringence, attenuation) that are similar to the target application. En face maps of peak fluorescence intensity (a) and average lifetime (b) demonstrate that consistent average lifetime values can be successfully extracted despite large variations of signal intensity. Cross sections are provided in two areas of the vessel (c/d: side branches, e/f: large vessel diameter) FLIm average lifetime encoded B-scans demonstrate uniform lifetime values. The OCT backscatter intensity image demonstrates clear visualization of media, adventitia, and perivascular tissue, with a penetration depth of at least 1 mm. High birefringence associated with high smooth muscle cell content is observed in the media (d, f). As expected, the demarcation between media and adventitia based on birefringence is less clear when the optical beam is crossing the media at a shallow angle (f, location marked with *): in that configuration, the muscle fibers are more closely aligned with the beam and thus birefringence is reduced. The depolarization is uniform and low due to the absence of lipid pools in healthy vessels (d, f). Display of mean and standard deviation of average lifetimes for the 380, 400 and 450 nm spectral bands shows a reduction of average lifetime as the wavelength increases (g). This finding is consistent with a relative increase in elastin-to-collagen fluorescence contribution at longer wavelength [15]. For each spectral band and intensity level, we also report a low standard deviation of the measured lifetime (~0.1 to 0.2 ns), which increases with decreasing intensity. A modest but very consistent reduction of the average lifetime with decreasing signal intensity was also observed (see discussion section).
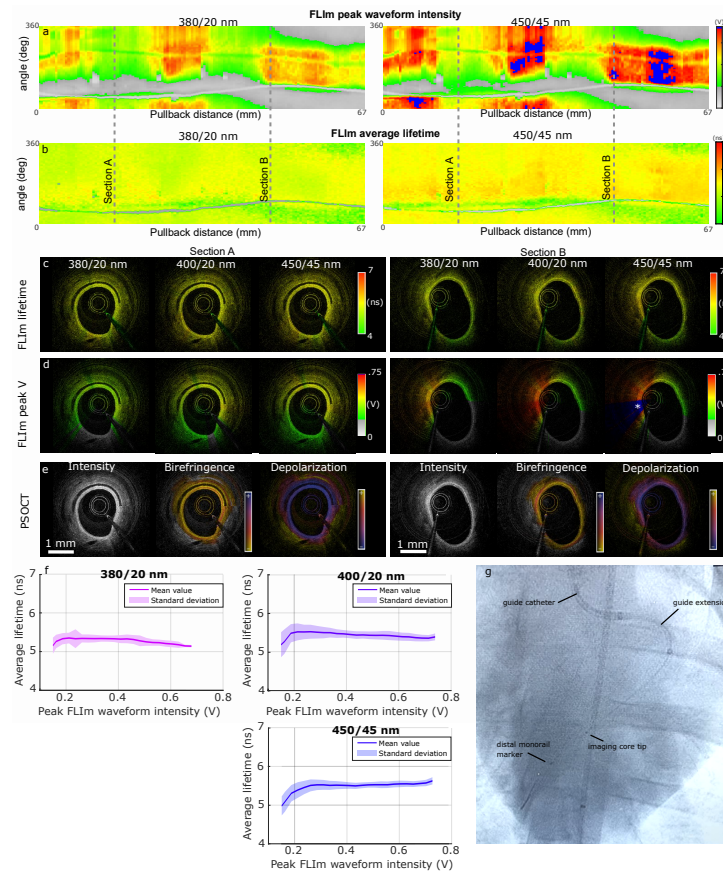
Fig. 6. *In vivo* **FLIm-PSOCT imaging of swine coronary artery segment.** The system's ability to acquire data in realistic conditions was validated by acquiring data in both left anterior descending and circumflex coronary arteries. En face images in the 370-nm and 450-nm bands demonstrate large variations of signal due to variations in probe to wall distance (a), but consistent lifetime values can be recovered as long as the peak signal voltage as above 0.2 V (b). Bimodal overlay showing average lifetime (c) and peak voltage (d) on OCT B-scans are provided for sections A and B. In section A, the smaller vessel diameter and close to centered position of the catheter in the lumen enables accurate lifetime measurement over the entire lumen circumference. In section B, areas of low signal led to an underestimation of the lifetime, whereas the saturated signal in the 450-nm band (location marked with *) does not seem to prevent accurate estimation of the lifetime. OCT intensity, birefringence and depolarization B-scans (e), provided for sections A and B, highlight the reduced vessel wall thickness in this young animal. The media birefringence is observed in both sections with, as expected, more contrast present in locations where the OCT beam is normal to the lumen. The evaluation of average lifetime versus signal intensity shows limited lifetime variability for intensities above approximately 0.2 V (f). This information is key to understand if variations of lifetime observed across the sample are driven by changes in composition or artifacts due to low signal. Fluoroscopy image demonstrating the placement of the catheter in the left anterior descending coronary artery (g).

4.　Discussion

Hybrid intravascular imaging systems play a key role in the assessment of a range of morphological and compositional features of various subtypes of atherosclerotic lesions [13,39]. This study demonstrates for the first time the integration of FLIm with PSOCT in a catheter system compatible with intracoronary investigations. PSOCT, an evolution of classical OCT [40], can provide valuable tissue-type related information in addition to microstructure by estimating depth-resolved birefringence and cumulative depolarization via measurement of the backscattered IR light polarization [21,22]. While PSOCT and combined FLIm-OCT devices were previously demonstrated independently, combining FLIm with PSOCT poses unique challenges due to the need for a broadband rotary junction and DCF catheters, which can affect the PSOCT performance. Additionally, the use of DCF presents the clear benefit of an additional optical channel facilitating multimodal imaging but leads to a degradation of OCT performance due to the introduction of multipath artifacts, that has not been discussed in earlier intravascular FLIm-OCT publications [18,19,38]. Specific technical developments and careful characterization of the system's performance were addressed in this study. High OCT image quality was made possible by a novel rotary junction design with high return losses. The FLIm spectral bands have also been optimized to support future clinical validation work. The system's ability to acquire data during percutaneous coronary intervention in animal demonstrated its robustness (push/pull, operation in tortuous path including sharp bending), reliability (>20 pullbacks were performed in two vessels without any malfunction) and ease of use (precise synchronization of pullback with flushing). These results establish that the proposed system can support future clinical validation of the technology

The combination of OCT and FLIm leverages the mature intravascular OCT technology and the robust rotational FLIm instrumentation developed earlier in support of clinical translation studies [25,41]. Both modalities can be integrated using a single double-clad fiber with dimensions identical to regular single-mode fibers, as demonstrated by a few earlier studies [18,19,38]. While the FLIm-PSOCT catheter system reported here differs from standard OCT due to the addition of polarization modulation of the light directed to the tissue and polarization-diverse detection, the current implementation can achieve similar A-scan rates as a standard OCT system. Thus, the system reported here has dimensions and characteristics similar to intravascular OCT systems used in patients [40]. It is capable of intravascular imaging at 100 B-scans/s, over up to 80 mm pullback length, and at a speed of up to 40 mm/s, with an imaging section presenting a low profile (2.7 Fr). Fast framerate and pullback speed are required because in the clinical setting, FLIm and OCT acquisitions need to be completed during a bolus injection of fluid that clears the artery segment for a short duration of ~3 to 5s. Because the proposed FLIm-PSOCT catheter's key characteristics (device size, acquisition speed) are similar to intravascular OCT systems currently used in clinical settings, we expect that this device will integrate seamlessly with standard PCI procedures, which is a key consideration to facilitate future validation of the technology in the catheterization laboratory.

A key contributor to OCT performance is to minimize unwanted reflections throughout the optical path. Even if not pathlength-matched, these can lead to spurious interference effects that impact the noise floor and limit system sensitivity. In intraluminal FLIm-PSOCT, the main source of these unwanted reflections is in the rotary collimator. We hypothesized that the combination of polarization-diverse detection and the specific cavity length of the employed laser source made the current system more susceptible to these reflections, compared to FLIm-OCT catheter systems reported in earlier studies [19,42]. Fiber optic rotary junctions (FORJ) suitable for single-mode transmission over a narrow wavelength range are routinely used in telecom, robotics, and medical imaging [43]. These implementations achieve high insertion and return losses by a combination of index matching fluid, antireflective coatings, low separation of rotary and stationary elements, and/or GRIN collimator to minimize the index mismatch at the

optical interfaces [43]. These standard solutions are not suitable for operation over extended wavelength ranges or when wavelength multiplexing is to be performed in the rotary junction's gap. Therefore, intraluminal OCT systems operating at non-standard wavelength [44], or OCT in combination with FLIm [18,19] or standard fluorescence [45,46] relied on low return loss fiber optic rotary junctions. The effect of unwanted back-reflection from these low return loss junctions on system noise has not been specifically reported, so the exact effect on imaging performance is unclear. Although low insertion losses and high return losses have been achieved using lensless designs [47,48], reliability and stability are a concern, and this concept has not seen wide adoption. In contrast, the FORJ reported in this study relies on a traditional lensed design, with the addition of a fused silica spacer placed in physical contact with the catheter fiber's proximal facet. In this design, the air/glass interface encountered by the infrared beam generating the unwanted back-reflection is located at the proximal end of the spacer, rather than the fiber core itself. Because the back-reflection is generated out of the focal plane, it is rejected in a similar fashion to confocal microscopy, with the stationary OCT fiber core acting as the pinhole. Since only a small fraction of the light reflected at the interface is coupled back into the OCT single-mode fiber, a return loss of 43 dB was achieved. This is a significant improvement compared to the 14 dB return loss typically observed for low return loss designs [43]].

Another potential performance limitation in FLIm/OCT multimodal systems stems from the crosstalk between inner cladding modes and the fundamental core mode of the catheter's DCF. This effect was evaluated and compared with results obtained from a standard OCT catheter relying on an SMF fiber. We observed that DCF artifacts, due to the propagation of the backscattered OCT signal in the inner cladding of the DCF are generated by the system's interfaces as well as objects within the field of view. In both cases, most of the artifact appears at a shorter path length determined by the length of the DCF and the core and inner cladding group refractive indices. Therefore, DCF artifacts generated by the light back-reflected at the exit surface of the imaging core are not expected to overlap with the signal measured from tissue (Fig. 3(a)-(c)). The adoption of an open sheath catheter design, where the inner cavity of the catheter is flushed with fluid, further reduces the exit surface artifact. Indeed, the index of water is closer to the index of fused silica used for the device's distal end, so a fluid-filled sheath leads to a reduction of the back-reflected power at this interface. In that configuration, we observed that the noise of the system is actually inferior to what was obtained with the reference SMF catheter.

DCF artifacts generated by objects in the field of view were also evaluated by imaging a 0.5 mm sheet of ABS. This material was chosen because it generates a signal intensity of approximately 30 dB (Fig. 3(b)), which is more realistic than the strong reflection obtained from a mirror, but higher than what is typically observed from the artery specimen (approximately 20 dB) and thus represents a worst-case condition. The DCF artifact induced by the object has a maximum intensity of approximately 10 dB. As with the exit surface artifact, this maximum is located proximal to the object by about 4 mm and therefore will not overlap with any other object in the field of view. DCF artifacts located in the imaging range have an amplitude of 2 to 4 dB and thus are not expected to degrade the image quality in a significant way, as illustrated in the artery specimen images (Fig. 5)

The multi-APD FLIm system design utilized in the current dual-modality system has been derived from our high-performance pulse-sampling-FLIm system designed for clinical research [25]. The system offers high detection sensitivity ($>3 \times 10^4$ V/W conversion gain), high lifetime measurement accuracy (< 200 ps standard deviation), and improved SNR (>50 dB) as a result of individual feedback gain adjustment for each spectral channel. The pulse-sampling lifetime measurement approach was chosen for intravascular application due to its high data acquisition speed compared to TCSPC which is the most commonly used method in fluorescence lifetime studies [49]. For fiber-based systems, the pulse sampling approach was shown to have an imaging speed 25 times faster than traditional TCSPC making it well-suited for intravascular applications

[24]. Adjustment of the detector gain is critical to acquire high SNR FLIm data. Practically, the detector gain should be set to maximize signal intensity throughout a scan while ensuring that the detector output does not exceed the digitizer's input range. However, real-time closed-loop control of the detector gains of each spectral channel, implemented in earlier FLIm systems designed for hand-held measurements to compensate for variations in probe-to-object distance and sample brightness [25], is not suitable for intravascular applications. This is due to the high point-measurement speed (30 kHz) and fast variations in signal intensity observed with a 100-rps catheter rotation speed. Thus, in this study, the gain of the photodetector for each individual spectral band was fixed for each pullback, where the optimal gain was determined by manually adjusting the gain of each APD detector based on trial imaging runs. An alternative future solution is to optimize the gain based on the FLIm intensity histogram so that the number of FLIm pixels with good SNR is maximized.

As expected, the ability to retrieve accurate fluorescence lifetime is influenced by the object's distance and tissue brightness. As distance increases, the fluorescence signal magnitude and SNR decrease, leading to a slight reduction in lifetime estimation accuracy, illustrated by the increase in lifetime standard deviation in both phantoms (Fig. S3), artery specimen (Fig. 5), and *in vivo* measurements (Fig. 6). Measurements in artery specimens also show a small but consistent reduction of average lifetime as the signal intensity decreases. Non-linearities in the FLIm system characteristics or artifacts due to data processing can be ruled out since the linearity of the system's temporal response with intensity was specifically tested [25] and results in cylindrical fluorescent phantom show a variation of average lifetime of less than 50 ps over the whole intensity range (Fig. S3). A possible explanation, to be investigated further, is that the relative amount of fluorescence emission of collagen and elastin, the main fluorophores present in a healthy vessel wall, may vary with excitation fluence and photobleaching, itself directly influenced by distance. Data acquired *in vivo*, where bleaching is expected to be less prevalent than *ex vivo* measurements, also demonstrates a much lower dependence of lifetime on signal intensity, further supporting an effect of fluence that will be investigated in further studies. Overall, this change in lifetime related to intensity is unlikely to be observed in measurements performed in diseased vessels that typically present a small outer diameter due to stenosis [7]. We also observe a difference in average lifetime between *in vivo* and *ex vivo* measurements. These differences are expected based on earlier comparison of in vivo and ex vivo acquired data [14], the difference in animal age between *ex vivo* specimen and the *in vivo* experiment, translating in different vessel morphology (medial layer thickness), may also contribute to the difference in FLIm signature.

The FLIm bands of the system were also adapted from earlier reported work to facilitate further investigation of the FLIm contrast. Based on earlier FLIm studies [7,17,50], the following fluorophores are expected to be detected in each spectral band as follows. Emissions from collagen, elastin, proteoglycans, and lipids (cholesterol, cholesteryl oleate, lipoproteins) are expected in the 390/40 nm band. Emissions from elastin, collagen, lipoproteins, and calcifications are expected in the 450/45 nm band. Emissions from ceroids and -to a lesser extent- structural proteins are expected in the 540/50 nm band and extend into the 630/50 nm band with lower signal intensity. Investigation of the FLIm signature of human artery specimens has demonstrated that macrophage foam cell presence could be identified from their ceroid content with high sensitivity and specificity (AUC = 0.94) based on the signal from the 540/50 nm spectral band alone [7]. On the other hand, the lifetime increase in the 390/40 nm band is associated with newly formed lesions [7] but it is unclear whether proteoglycans, type III collagen, lipids, or other species present in these lesions [2,51,52] are at the origin of this observed FLIm contrast. To support further investigation, the 390/40 band used in earlier systems from our group [17,19] and other research groups in this field [16,18] was split into 380/20 and 400/20 bands to improve the spectral specificity and facilitate discrimination between these various constituents.

In conclusion, we developed an intravascular FLIm-PSOCT catheter system that provides morphology, microstructure, and biochemical composition information. The ability to acquire robust FLIm data as well as birefringence and depolarization via a DCF imaging catheter was confirmed in phantoms, coronary specimens, and *in vivo* in coronary percutaneous intervention in a swine. The ability to acquire in vivo data during PCI procedures demonstrates the reliability and performance of the system to in harsh use conditions. Overall, the current results demonstrate that this intravascular imaging platform is a promising tool for the investigation of inflammatory activity, where the high FLIm sensitivity and specificity [7], combined with depth resolution provided by OCT may prove valuable to ensure better quantification. Additionally, the reported system's improved FLIm spectral specificity in the 370 to 410 nm range, combined with the ability of PSOCT to provide information about collagen presence in the ECM may improve our understanding of the specific lesion components identified by FLIm.

Disclosures. The authors declare that there are no conflicts of interest related to this article.

Data availability. Data underlying the results presented in this paper are not publicly available at this time but may be obtained from the authors upon reasonable request.

Supplemental document. See Supplement 1 for supporting content.

References

1. S. S. Virani, A. Alonso, H. J. Aparicio, *et al.*, "Heart disease and stroke statistics—2021 update," Circulation **143**(8), E254–E743 (2021).
2. J. F. Bentzon, F. Otsuka, R. Virmani, *et al.*, "Mechanisms of plaque formation and rupture," Circ. Res. **114**(12), 1852–1866 (2014).
3. F. Otsuka, M. C. A. Kramer, P. Woudstra, *et al.*, "Natural progression of atherosclerosis from pathologic intimal thickening to late fibroatheroma in human coronary arteries: a pathology study," Atherosclerosis **241**(2), 772–782 (2015).
4. R. Virmani, A. P. Burke, A. Farb, *et al.*, "Pathology of the vulnerable plaque," J. Am. Coll. Cardiol. **47**(8 Suppl), C13–C18 (2006).
5. C. V. Bourantas, F. A. Jaffer, F. J. Gijsen, *et al.*, "Hybrid intravascular imaging: recent advances, technical considerations, and current applications in the study of plaque pathophysiology," Eur. Heart J. **38**(6), 400–412 (2017).
6. M. Seguchi, A. Aytekin, T. Lenz, *et al.*, "Intravascular molecular imaging: translating pathophysiology of atherosclerosis into human disease conditions," Eur. Heart J. Cardiovasc. Imaging **24**(1), e1–e16 (2022).
7. J. Bec, D. Vela, J. E. Phipps, *et al.*, "Label-free visualization and quantification of biochemical markers of atherosclerotic plaque progression using intravascular fluorescence lifetime," JACC: Cardiovascular Imaging **14**(9), 1832–1842 (2021).
8. H. Khraishah and F. A. Jaffer, "Intravascular molecular imaging: near-infrared fluorescence as a new frontier," Front. Cardiovasc. Med. **7**, 1–13 (2020).
9. G. J. Ughi, H. Wang, E. Gerbaud, *et al.*, "Clinical characterization of coronary atherosclerosis with dual-modality OCT and near-infrared autofluorescence imaging," J. Am. Coll. Cardiol. Img. **9**, 1304–1314 (2016).
10. C. M. Gardner, H. Tan, E. L. Hull, *et al.*, "Detection of lipid core coronary plaques in autopsy specimens with a novel catheter-based near-infrared spectroscopy system," JACC: Cardiovascular Imaging **1**(5), 638–648 (2008).
11. A. M. Fard, P. Vacas-Jacques, E. Hamidi, *et al.*, "Optical coherence tomography – near infrared spectroscopy system and catheter for intravascular imaging," Opt. Express **21**(25), 30849 (2013).
12. R. Virmani, F. D. Kolodgie, A. P. Burke, *et al.*, "Atherosclerotic plaque progression and vulnerability to rupture: angiogenesis as a source of intraplaque hemorrhage," Arterioscler., Thromb., Vasc. Biol. **25**(10), 2054–2061 (2005).
13. A. Ramasamy, P. W. Serruys, and D. A. Jones, "Reliable in vivo intravascular imaging plaque characterization: a challenge unmet," Am. Heart J. **218**, 20–31 (2019).
14. L. Marcu, J. A. Jo, Q. Fang, *et al.*, "Detection of rupture-prone atherosclerotic plaques by time-resolved laser-induced fluorescence spectroscopy," Atherosclerosis **204**(1), 156–164 (2009).
15. Y. Sun, Y. Sun, D. Stephens, *et al.*, "Dynamic tissue analysis using time- and wavelength-resolved fluorescence spectroscopy for atherosclerosis diagnosis," Opt. Express **19**(5), 3890–3901 (2011).
16. S. Kim, H. S. Nam, M. W. Lee, *et al.*, "Comprehensive assessment of high-risk plaques by dual-modal imaging catheter in coronary artery," JACC: Basic to Translational Science **6**(12), 948–960 (2021).

17. J. Bec, J. E. Phipps, D. Gorpas, *et al.*, "In vivo label-free structural and biochemical imaging of coronary arteries using an integrated ultrasound and multispectral fluorescence lifetime catheter system," Sci. Rep. **7**(1), 8960 (2017).
18. M. W. Lee, J. W. Song, W. J. Kang, *et al.*, "Comprehensive intravascular imaging of atherosclerotic plaque in vivo using optical coherence tomography and fluorescence lifetime imaging," Sci. Rep. **8**(1), 14561 (2018).
19. C. Li, J. Bec, X. Zhou, *et al.*, "Dual-modality fluorescence lifetime imaging-optical coherence tomography intravascular catheter system with freeform catheter optics," J. Biomed. Opt. **27**, 076005 (2022).
20. Z. A. Ali, K. K. Galougahi, G. S. Mintz, *et al.*, "Intracoronary optical coherence tomography: State of the art and future directions," EuroIntervention **17**(2), e105–e123 (2021).
21. M. Villiger, K. Otsuka, A. Karanasos, *et al.*, "Coronary plaque microstructure and composition modify optical polarization: a new endogenous contrast mechanism for optical frequency domain imaging," JACC: Cardiovascular Imaging **11**(11), 1666–1676 (2018).
22. K. Otsuka, M. Villiger, A. Karanasos, *et al.*, "Intravascular polarimetry in patients with coronary artery disease," JACC: Cardiovascular Imaging **13**(3), 790–801 (2020).
23. J. Han, S. Kim, H. Jung Kim, *et al.*, "Label-free characterization of atherosclerotic plaques via high-resolution multispectral fluorescence lifetime imaging microscopy," Arterioscler., Thromb., Vasc. Biol. **43**(7), 1295–1307 (2023).
24. X. Zhou, J. Bec, K. Ehrlich, *et al.*, "Pulse-sampling fluorescence lifetime imaging: evaluation of photon economy," Opt. Lett. **48**(17), 4578 (2023).
25. X. Zhou, J. Bec, D. Yankelevich, *et al.*, "Multispectral fluorescence lifetime imaging device with a silicon avalanche photodetector," Opt. Express **29**(13), 20105 (2021).
26. J. Bec, C. Li, and L. Marcu, "Broadband, freeform focusing micro-optics for a side-viewing imaging catheter," Opt. Lett. **44**(20), 4961 (2019).
27. J. Liu, Y. Sun, J. Qi, *et al.*, "A novel method for fast and robust estimation of fluorescence decay dynamics using constrained least-squares deconvolution with Laguerre expansion," Phys. Med. Biol. **57**(4), 843–865 (2012).
28. M. Villiger, E. Z. Zhang, S. K. Nadkarni, *et al.*, "Spectral binning for mitigation of polarization mode dispersion artifacts in catheter-based optical frequency domain imaging," Opt. Express **21**(14), 16353 (2013).
29. National Research Council (U.S.) Committee for the Update of the Guide for the Care and Use of Laboratory Animals, Institute for Laboratory Animal Research (U.S.), and National Academies Press (U.S.), *Guide for the Care and Use of Laboratory Animals* (National Academies Press, 2011).
30. *IEC 60825-1:2014/ISH2:2017* (2014).
31. P. R. T.-P.-14-0012. ANSI Z136.1, "Safe Use of Lasers," Laser Institute of America – laser applications and safety (2014).
32. K. Beaudette, H. W. Baac, W.-J. Madore, *et al.*, "Laser tissue coagulation and concurrent optical coherence tomography through a double-clad fiber coupler," Biomed. Opt. Express **6**(4), 1293 (2015).
33. A. Tanskanen, G. Hohert, A. Lee, *et al.*, "Higher-order core-like modes in double-clad fiber contribute to multipath artifacts in optical coherence tomography," J. Lightwave Technol. **39**(17), 5573–5581 (2021).
34. X. Lian, G. Farrell, Q. Wu, *et al.*, "Mode transition in conventional step-index optical fibers," *2019 18th International Conference on Optical Communications and Networks* (2019).
35. X. Lian, Q. Wu, G. Farrell, *et al.*, "Discrete self-imaging in small-core optical fiber interferometers," J. Lightwave Technol. **37**(9), 1873–1884 (2019).
36. M. Villiger, K. Otsuka, A. Karanasos, *et al.*, "Repeatability assessment of intravascular polarimetry in patients," IEEE Trans. Med. Imaging **37**(7), 1618–1625 (2018).
37. X. Liu, K. Beaudette, X. Wang, *et al.*, "Tissue-like phantoms for quantitative birefringence imaging," Biomed Opt. Express **8**(10), 4454 (2017).
38. X. Chen, W. Kim, M. J. Serafino, *et al.*, "Dual-modality optical coherence tomography and frequency-domain fluorescence lifetime imaging microscope system for intravascular imaging," J. Biomed. Opt. **25**(01), 1–14 (2019).
39. M. Michail, P. W. Serruys, R. Stettler, *et al.*, "Intravascular multimodality imaging: feasibility and role in the evaluation of coronary plaque pathology," Eur. Heart J. Cardiovasc. Imaging **18**(6), 613–620 (2017).
40. V. Subban and O. C. Raffel, "Optical coherence tomography: Fundamentals and clinical utility," Cardiovasc. Diagn. Ther. **10**(5), 1389–1414 (2020).
41. M. J. Serafino, B. E. Applegate, and J. A. Jo, "Direct frequency domain fluorescence lifetime imaging using field programmable gate arrays for real time processing," Rev. Sci. Instrum. **91**, 033708 (2020).
42. B. E. Sherlock, X. Zhou, J. Bec, *et al.*, "Synchronous fluorescence lifetime imaging and optical coherence tomography using a double clad fiber," in *2016 IEEE Photonics Conference, IPC 2016* (2017), Vol. 42, pp. 3753–3756.
43. *Fiber Optic Rotary Joints (FORJ) - Performance and Application Highlights White Paper* (n.d.).
44. H.-C. Park, J. Mavadia-Shukla, W. Yuan, *et al.*, "Broadband rotary joint for high-speed ultrahigh-resolution endoscopic OCT imaging at 800 nm," Opt. Lett. **42**(23), 4978–4981 (2017).
45. S. Lee, M. W. Lee, H. S. Cho, *et al.*, "Fully integrated high-speed intravascular optical coherence tomography/near-infrared fluorescence structural/molecular imaging in vivo using a clinically available near-infrared fluorescence–emitting indocyanin," Circ: Cardiovascular Interventions **7**(4), 560–569 (2014).
46. H. Yoo, J. W. Kim, M. Shishkov, *et al.*, "Intra-arterial catheter for simultaneous microstructural and molecular imaging in vivo," Nat. Med. **17**(12), 1680–1684 (2011).

47. W. Kim, X. Chen, J. A. Jo, *et al.*, "Lensless, ultra-wideband fiber optic rotary joint for biomedical applications," Opt. Lett. **41**(9), 1973 (2016).
48. Tearney, "Systems and methods for providing an optical rotary joint," U.S. patent US 10,845,546 (2020).
49. J. R. Lakowicz, *Principles of Fluorescence Spectroscopy* (Springer, 2011).
50. L. Marcu, D. Cohen, J.-M. I. Maarek, *et al.*, "Characterization of type I, II, III, IV, and V collagens by time-resolved laser-induced fluorescence spectroscopy," Proc. SPIE **3917**, 93–101 (2000).
51. I. K. Jang, "Plaque progression: Slow linear or rapid stepwise?" Circ. Cardiovasc. Imaging **10**(9), e006964 (2017).
52. R. Vergallo and F. Crea, "Atherosclerotic plaque healing," N. Engl. J. Med. **383**(9), 846–857 (2020).